JEM Journal of Experimental Medicine

TECHNICAL ADVANCES AND RESOURCES

B cell dissemination patterns during the germinal center reaction revealed by whole-organ imaging

Liat Stoler-Barak[1], Adi Biram[1], Natalia Davidzohn[1], Yoseph Addadi[2], Ofra Golani[2], and Ziv Shulman[1]

Germinal centers (GCs) are sites wherein B cells proliferate and mutate their immunoglobulins in the dark zone (DZ), followed by affinity-based selection in the light zone (LZ). Here, we mapped the location of single B cells in the context of intact lymph nodes (LNs) throughout the GC response, and examined the role of BCR affinity in dictating their position. Imaging of entire GC structures and proximal single cells by light-sheet fluorescence microscopy revealed that individual B cells that previously expressed AID are located within the LN cortex, in an area close to the GC LZ. Using in situ photoactivation, we demonstrated that B cells migrate from the LZ toward the GC outskirts, while DZ B cells are confined to the GC. B cells expressing very-low-affinity BCRs formed GCs but were unable to efficiently disperse within the follicles. Our findings reveal that BCR affinity regulates B cell positioning during the GC response.

Introduction

Generation of protective antibodies is crucial for clearance of harmful pathogens and for establishment of long-lasting immunological memory (Victora and Nussenzweig, 2012; De Silva and Klein, 2015). In response to vaccination or invading microbes, antigen-specific B cells within secondary lymphoid organs differentiate into antibody-producing cells or early memory cells or rapidly proliferate and form structures known as germinal centers (GCs; Allen et al., 2007). The main purpose of the GC response is to produce long-lived plasma cells (PCs) that secrete high-affinity antibodies, and memory cells that can readily elicit an efficient antibody immune response upon re-exposure to the immune stimuli (Corcoran and Tarlinton, 2016; Weisel and Shlomchik, 2017). GCs are divided anatomically into two distinct functional zones based on the B cell density, as well as the presence of zone-specific cellular assemblies (MacLennan, 1994; Heesters et al., 2014). In the dark zone (DZ), B cells rapidly proliferate and insert mutations into their Ig variable regions followed by migration to the GC light zone (LZ), where they interact with antigen and compete for T cell help (Allen et al., 2007; Victora et al., 2010). Iterative cycles of B cells between the GC zones lead to accumulation of affinity-enhancing mutations and ultimately to progressive increase in serum antibody affinity, a process known as antibody affinity maturation (Eisen and Siskind, 1964; Jacob et al., 1991).

During the GC reaction, rare B cell subsets express surface markers that identify pre-memory cells as well as transcription factors that promote the generation of pre-PCs such as Irf4 and Blimp-1 (Kräutler et al., 2017; Laidlaw et al., 2017; Suan et al., 2017a; Wang et al., 2017). PC-related markers are widely used to detect PCs positioned outside the GC structure by imaging techniques, and lineage-specific markers on non-GC class switched B cell subsets are used to detect memory cells by flow cytometry techniques (Mohr et al., 2009; Fooksman et al., 2010; Meyer-Hermann et al., 2012; Kräutler et al., 2017; Zhang et al., 2018). It was shown that PCs are found in the proximity of the GC DZ, and Blimp-1$^+$ or CD138$^+$ cells were demonstrated to traverse through the T zone to the LN medullary cords at early stages of the B cell response (Fooksman et al., 2010; Meyer-Hermann et al., 2012; Zhang et al., 2018). However, the position and the path taken by GC-derived PCs at later stages of the response are less clear. In addition, it was demonstrated that few memory B cells are positioned next to contracting GCs and next to the subcapsular sinus, where they can rapidly respond to antigen upon re-exposure (Aiba et al., 2010; Suan et al., 2017a; Moran et al., 2018). Nonetheless, since these cells have no clear markers for imaging analysis during the GC reaction, detecting post-GC cells remains a challenge. Furthermore, cells that are not fully differentiated and do not express typical memory and PC markers are expected to emerge during the GC reaction (Kallies et al., 2004; Wang et al., 2017).

Most of the data that examined the location of activated B cells in LNs and spleen were generated by traditional two-dimensional cross sections or by in situ intravital imaging that provided critical information about the GC structures and

[1]Department of Immunology, Weizmann Institute of Science, Rehovot, Israel; [2]Life Sciences Core Facilities, Weizmann Institute of Science, Rehovot, Israel.

Correspondence to Ziv Shulman: ziv.shulman@weizmann.ac.il.

positioning of single cells. However, these techniques visualize a limited number of immunological niches and do not capture the entire GC structure (Wittenbrink et al., 2011). Furthermore, visualization of the entire niche structure in combination with rare individual cells in the context of an intact organ is nearly impossible by using these methods. Thus, in order to obtain a complete map of the B cell response, including all of the GC structures as well as the position of single cells, a novel large-scale imaging technique is required (Biram et al., 2019).

Although T cells select B cells for clonal expansion and PC formation in the GC, how B cell receptor (BCR) affinity regulates positioning of individual B cells in different microanatomical sites is unclear. Here, we used a whole-organ imaging and pulse-chase approaches for mapping the position of single B cells in the context of an intact organ throughout the GC reaction. We found that BCR affinity regulates B cell entry into, and dissemination within, the LN cortex during the GC response.

Results

Whole-organ imaging captures all the GC structures and single activated B cells in intact LNs

To examine and compare variations among all GC structures over time in the context of an intact LN during a polyclonal immune response, we combined fate reporter mice with a whole-organ imaging approach using light-sheet fluorescence microscopy (LSFM; Biram et al., 2019). The enzyme activation-induced cytidine deaminase (AID) is expressed in early-responding B cells before GC coalescence and during the GC reaction (Crouch et al., 2007; Rommel et al., 2013). To determine whether a cell is located within the GC, most studies use typical memory and PC markers that define the cell identity. To examine all the responding B cells, including cells that are not part of the GC response, we used a technique that allows detection of cell position in intact LNs, independently of specific lineage markers. For this purpose, we used a fate reporter mouse model in which B cells express the tdTomato fluorescent protein, induced during and after expression of AID ($AID^{Cre/+}.Rosa26^{lox\text{-}stop\text{-}lox\text{-}tdTomato/+}$, referred to as AID.Cre.tdTomato; Kaji et al., 2012; Taylor et al., 2012). AID.Cre.tdTomato mice were immunized by injection of OVA coupled to the hapten 4-hydroxy-3-nitrophenylacetyl (NP-OVA) precipitated in alum into the hind footpads. Popliteal LNs were dissected at different time points, fixed, and subjected to clarity protocols followed by LSFM imaging (Fig. S1). To visually distinguish between very bright GC structures and dimmer individual cells, we used an artificial volumetric and intensity-based color-encoded image presentation that allows clear visualization of less bright single cells (Fig. 1 A and Materials and methods). Whereas no tdTomato$^+$ B cells and no GCs were detected in unimmunized mice, starting 3 d after immunization, single tdTomato$^+$ B cells and small clusters of cells were detected throughout the LN cortex (Fig. 1, A–D). At the peak of the GC response, 12–14 d after initial immunization, 10–16 individual GCs were observed within single popliteal LNs (Fig. 1, A and B; and Video 1). Similar results were observed in mice challenged with a more complex antigen than a hapten (chicken gamma globulin) or infected with vesicular stomatitis virus (VSV; Fig. S2 A). Immunohistochemical analysis of tdTomato$^+$ clusters confirmed that these were typical GCs with B cells that express the GC marker GL-7 (Fig. S2 B). Quantification of the number of GCs in 28 intact LNs over time revealed small changes in GC number between days 7 and 20 after initial immunization, followed by a 1.5-fold decline on day 28 (Fig. 1, A and B). The volume of single GCs was highly heterogeneous, with some GCs that were less than 0.2×10^7 μm^3 in size, and some as large as 1.5×10^7 μm^3 at the peak of the response (Fig. 1 C). The maximal average size of the GCs was at days 12–14 after immunization, followed by 4.15-fold reduction after an additional 14–16 d (Fig. 1 C). Integration of the GC number (11.6 on days 12–14 and 8 on day 28) and GC volume (0.43×10^7 μm^3 on days 12–14 and 0.10^7 μm^3 on day 28) parameters showed that the number of total GC cells per LN was reduced 6.2-fold between the peak of the response and day 28 (Fig. 1, B and C). Thus, whereas the GC number per LN is relatively stable, the size of the GCs within intact LNs is highly variable and declines over time.

The LSFM technique allowed us to visualize and quantify the absolute number of single cells within the LN, located outside the GC structures. This cell population consists of B cells that originate from the GC, as well as B cells that expressed AID but never took part in the GC reaction. Quantification of single tdTomato$^+$ cells in individual LNs over time revealed ∼5,200 B cells on average in the LN follicles on day 3 after immunization, and this number was increased to 9,451 cells, on average, 4 d later (Fig. 1 D). The maximal number of tdTomato$^+$ single cells outside the GC structures was detected 12–14 d after initial immunization, with a 2.5-fold increase in total cell number compared with day 7 (23,737 single cells, on average on days 12–14; Fig. 1 D). Notably, on days 12–14, the GC was at its maximal size as well, and fewer single cells were observed on day 20 when the GC size was reduced (Fig. 1, C and D). By 4 wk after the immunization, the number of single cells within the LN was dramatically reduced, as the GC response was diminished (Fig. 1, A–D). Remarkably, reduction in single cell number outside the GC structures over time was roughly similar to the change observed in GC size (threefold and 2.5-fold reduction in single cell number and GC size between days 12–14 to day 20, respectively). Normalization of the number of single cells to the total GC volume at different time points at which clear GC structures were detected revealed that this ratio did not significantly change over time (Fig. 1 E). Thus, during the immune response progression, both the GC size and the number of single cells throughout the LNs are reduced, suggesting that the magnitude of the GC response affects the pool of cells located outside the GC structures.

Single B cells that previously expressed AID are primarily positioned within the LN cortex during the GC reaction

To determine more precisely the position of single B cells that previously expressed AID in different microanatomical sites, we introduced landmarks into AID.Cre.tdTomato reporter mice, by labeling either the B cell follicles in the LN cortex or the T zone in the LN paracortex. To this end, naive CFP$^+$ B cells and GFP$^+$ T cells were co-transferred into immunized AID.Cre.tdTomato mice before LN dissection and imaging by LSFM. Whole-organ

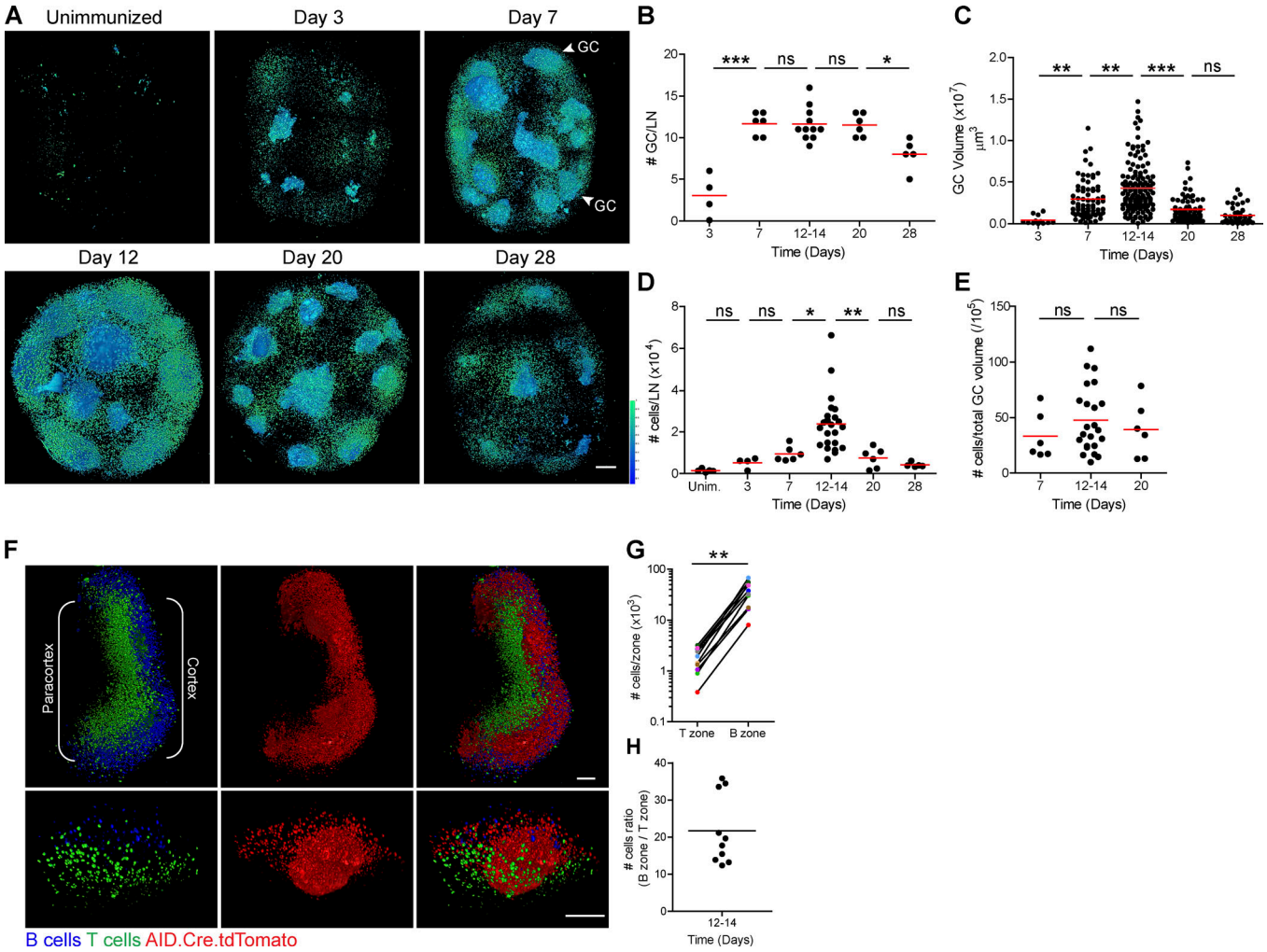

Figure 1. **Time-course analysis of all the GC structures and position of single B cells in intact LNs. (A)** Mice were immunized with NP-OVA, and popliteal LNs were dissected at different time points and imaged by LSFM. Representative 3D-rendered images in volumetric and rainbow visualization modes are shown. Scale bar, 200 µm. **(B–D)** Quantification of GC number per LN (B), GC volume (C), and number of single cells per LN (D). **(E)** The number of total single cells per LN normalized to the total GC volume at different time points. Data for A–E were pooled from 3–7 independent experiments with a total of 4–23 LNs from 3–16 mice per group. *, P < 0.05; **, P < 0.01; ***, P < 0.0001; ns, not significant; one-way ANOVA with Tukey's multiple comparisons test. **(F)** AID.Cre.tdTomato mice received GFP$^+$ T cells and CFP$^+$ B cells 12–14 d after immunization with NP-OVA. Representative 3D-rendered images of an LN and a single GC are shown. Scale bars, 200 µm (top panel); 100 µm (bottom panel). **(G)** Quantification of the number of individual tdTomato$^+$ B cells in the T zone and in B cell follicles in single LNs after GC exclusion. Each pair of colored dots represents a single LN. **, P < 0.01; Wilcoxon matched-pairs signed rank two-tailed test. **(H)** The ratio of the number of individual tdTomato$^+$ B cells in the B zone versus the T zone in individual LNs. Representative images and data for F–H were pooled from three independent experiments using a total of 10 LNs from eight mice. Unim., unimmunized.

imaging revealed that tdTomato$^+$ clusters of GC B cells were clearly found in the LN cortex, and some GCs were observed to come in contact with the T zone in the paracortex (Fig. 1 F). Furthermore, most of the tdTomato$^+$ single cells were detected throughout the cortex area, very close to the GC structures, whereas significantly fewer B cells were detected in the T zone (Fig. 1 F). This observation was not a result of inefficient detection of the fluorescent signal in the mid-LN area, as GFP$^+$ T cells were clearly visualized in the T zone, and analysis of half an LN in which the paracortex is located close to the microscope lens showed a similar cellular distribution pattern (Fig. S3 and Video 2). For quantification of single tdTomato$^+$ cells within each zone, an area of interest was generated based on the landmarks that were introduced into the mice, and the exact number of single tdTomato$^+$ cells was enumerated within each area in multiple LNs. This analysis revealed that most of the single tdTomato$^+$ B cells were located in the LN cortex, and 22-fold fewer tdTomato$^+$ B cells were found in the LN paracortex area at days 12–14, during the peak of the GC reaction (Fig. 1, G and H). Thus, we conclude that the majority of the individual B cells that previously expressed AID accumulate in the LN cortex rather than in the T zone.

GC-derived B cells accumulate in the LN cortex

Our initial findings demonstrated a correlation between GC size and the number of total individual B cells detected in intact LNs throughout the B cell response, suggesting a link between the number of single cells and the magnitude of the GC reaction.

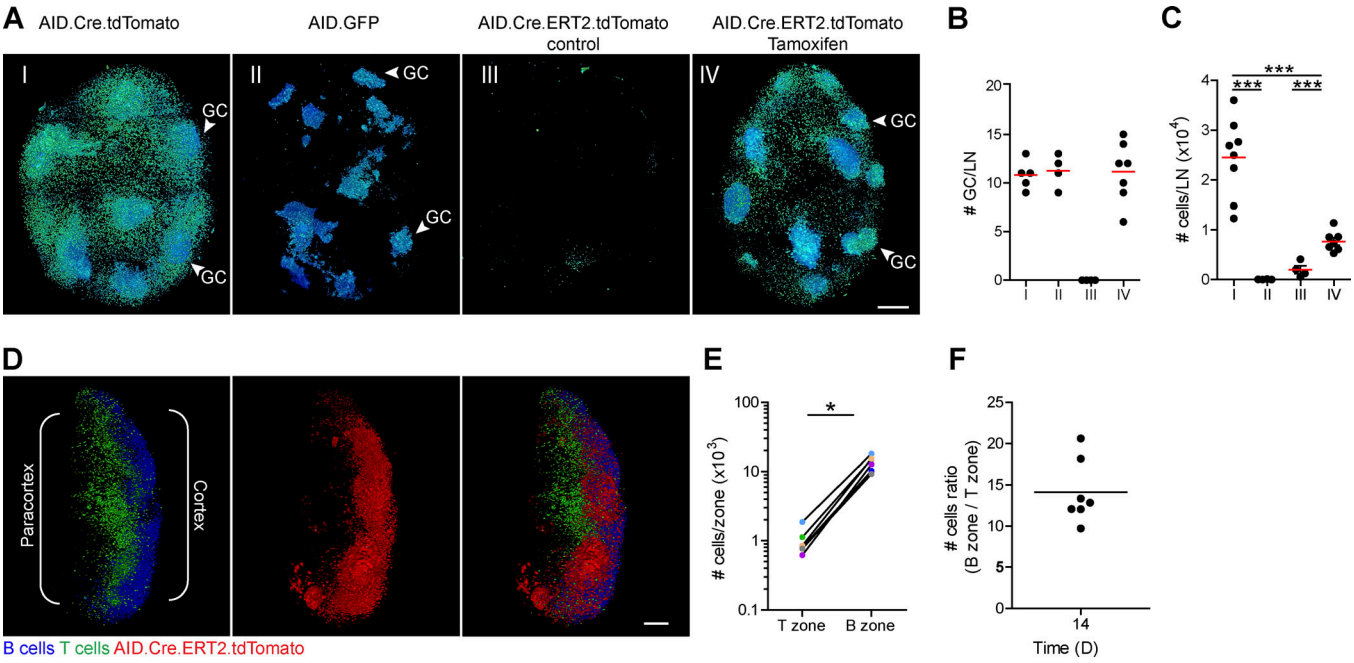

Figure 2. **The majority of the GC-derived B cells enter the LN cortex. (A)** LSFM 3D-rendered images of LNs removed from AID.Cre.tdTomato, AID-GFP, or AID.Cre.ERT2.tdTomato mice 12–14 d after immunization with NP-OVA. AID.Cre.ERT2.tdTomato mice were treated with either oil control or tamoxifen for 4 d. Scale bar, 200 µm. **(B and C)** GC number per LN (B) and number of individual non-GC cells per LN (C). Representative images and pooled data for A–C from two to five independent experiments with a total of four to eight LNs from four mice per group. ***, $P < 0.0001$; one-way ANOVA with Tukey's multiple comparisons test. **(D)** Tamoxifen-treated AID.Cre.ERT2.tdTomato mice that received GFP⁺ T cells and CFP⁺ B cells 14 d after immunization with NP-OVA. Representative 3D-rendered images of an LN are shown. Scale bar, 200 µm. **(E)** Quantification of the number of individual tdTomato⁺ B cells in the T zone and in B cell follicles in single LNs after GC exclusion. Each pair of colored dots represents a single LN. *, $P < 0.05$; Wilcoxon matched-pairs signed rank two-tailed test. **(F)** The ratio of the number of individual tdTomato⁺ B cells in the B zone versus the T zone in individual LNs. Representative images and data were pooled for D–F from three independent experiments using a total of seven LNs from five mice.

However, AID is expressed by antigen-specific B cells before GCs are formed (Fig. 1 A), and these have the potential to contribute to the pool of single cells in the LN cortex (Sze et al., 2000; Zhang et al., 2017). Therefore, it was impossible to distinguish between B cells that previously expressed AID and entered the follicles at early time points after immunization and B cells that accumulated in the LN cortex during the peak of the response when AID is expressed primarily by GC B cells. To address this problem, we used a "pulse-chase" strategy wherein AID-expressing B cells were labeled late during the B cell response after GC coalescence, at a time point when AID-expressing cells are expected to reside exclusively in the GC site. First, we verified this assumption in our system by comparing AID.Cre.tdTomato fate reporter mice to mice that express GFP fused to AID (AID.GFP), wherein GFP-positive cells represent B cells expressing AID at the specific time point of the analysis. Whole-organ imaging of LN derived from AID.GFP reporter mice revealed that on day 12 after immunization, GFP⁺ B cells were detected in GC clusters, and nearly no GFP⁺ single cells were found outside the GCs (Fig. 2, A–C). For tracking B cells that express AID late during the GC response, we used an additional AID reporter mouse strain, in which AID-expressing cells may be induced to express tdTomato at the peak of the GC reaction. To this end, we bred Rosa26$^{lox\text{-}stop\text{-}lox\text{-}tdTomato/+}$ to AID.Cre.ERT2 mice to produce mice in which tdTomato is expressed in AID-positive cells only after administration of tamoxifen. Whole-organ imaging by LSFM of intact LNs from immunized AID.Cre.ERT2.tdTomato mice revealed that no GC structures were evident without tamoxifen treatment (Fig. 2, A and B). To specifically label AID-expressing B cells during the peak of the GC reaction, and not early activated B cells, mice were treated with tamoxifen on day 10 after immunization, and dissected LNs were examined 4 d later by LSFM and flow cytometry. Analysis of cell suspensions derived from LNs of these reporter mice revealed that recombination and tdTomato⁺ expression took place in nearly all the GC cells after treatment with tamoxifen (~98%), and LSFM imaging revealed that the number of individual GCs in intact LNs was similar among the different AID reporter mice (Fig. 2, A and B; and Videos 1 and 3). Individual tdTomato⁺ cells were detected within intact LNs of AID.Cre.ERT2.tdTomato mice, primarily within the cortex area; however, their number per LN was threefold lower than observed in AID.Cre.tdTomato mice (Fig. 2 C). Similarly to the data obtained using AID.Cre.tdTomato mice, in AID.Cre.ERT2.tdTomato mice, most of the single tdTomato⁺ B cells were located in the LN cortex area, and significantly fewer tdTomato⁺ B cells were found in the LN paracortex area at day 14 after immunization (Fig. 2, D–F). Thus, together with our initial observations, we conclude that the majority of B cells that expressed AID at the peak of the GC response, including GC B cells, accumulate primarily in the LN cortex.

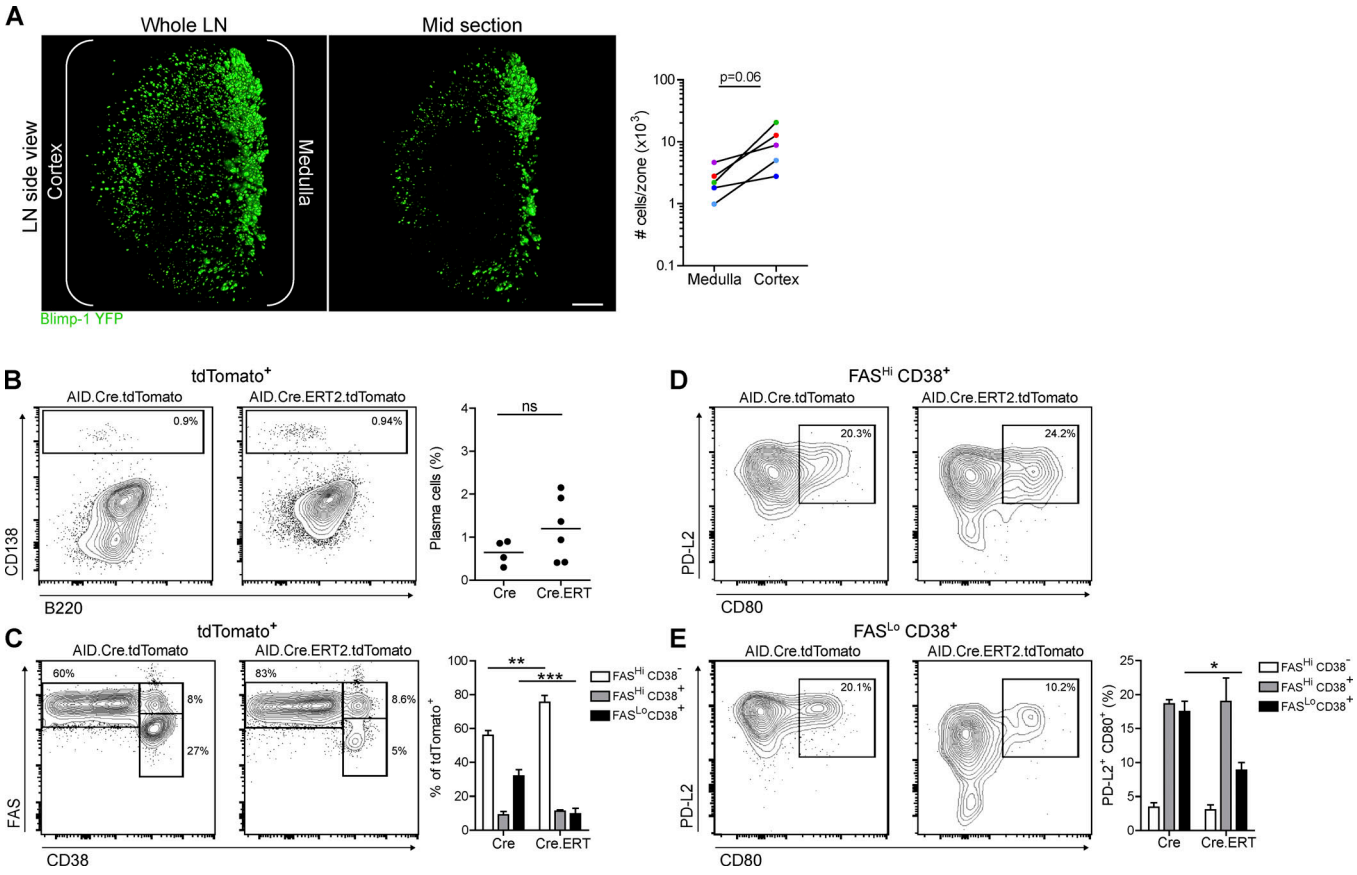

Figure 3. **PC position in LNs and lineage markers of individual non-GC B cells at the peak of the GC response. (A)** LSFM 3D-rendered images of LNs removed from Blimp-1-YFP mice 12 d after immunization with NP-OVA, and quantification of the number of individual Blimp-1 YFP B cells in the cortex or medulla in single LNs after GC exclusion. Each pair of colored dots represents a single LN. P = 0.06; Wilcoxon matched-pairs signed rank two-tailed test. Scale bar, 200 µm. **(B)** Representative flow cytometric plots and quantification of PCs ($CD138^+$) in AID.Cre.tdTomato (left; Cre) or AID.Cre.ERT2.tdTomato (right; Cre.ERT) mice 14 d after immunization with NP-OVA, within the $tdTomato^+$ B cell population. ns, not significant; two-tailed Student's *t* test. **(C)** Representative flow cytometric plots and quantification of FAS^{Hi} $CD38^-$ (GC cells), FAS^{Hi} $CD38^+$, and FAS^{Lo} $CD38^+$ (non-GC cells). **(D and E)** Representative flow cytometry plots and quantification of memory cells ($PD\text{-}L2^+$ $CD80^+$) in $tdTomato^+$ cells 14 d after immunization with NP-OVA, within the FAS^{Hi} $CD38^+$ and FAS^{Lo} $CD38^+$ B cell population. Data pooled for B–E from two independent experiments with a total of four to six mice per group. Data are represented as means ± SEM. *, P < 0.05; **, P < 0.01; ***, P < 0.0001; one-way ANOVA with Tukey's multiple comparisons test.

LN localization of PCs and lineage markers of tdTomato-expressing B cells

To examine the location of PCs within the LN, mice that express YFP under the PC transcription factor promoter Blimp-1 were immunized with NP-OVA. LSFM imaging revealed Blimp-1 YFP^+ cells in large clusters in the medullary region of the LN, and individual Blimp-1 YFP^+ cells were detected throughout the LN cortex (Fig. 3 A). Quantification of cell numbers in the different microanatomical sites revealed that although many PCs are clustered next to the LN vertical area, most of the individual cells were scattered throughout the LN cortex, and very few cells were detected in the mid part of the LN (Fig. 3 A). These findings were not affected by ineffective signal detection in the mid part of the LN, since we demonstrated that our technique can detect cells in this area (Fig. 1 G and Fig. 2 E). These observations corroborated our findings in AID reporter mice. We conclude that during the peak of the response, PCs are located primarily in the cortex and medullary area of the LN.

To compare flow-based techniques and the imaging approach of the non-GC cell population in the LNs, we examined the expression of typical PC and memory markers of immunized AID.Cre.tdTomato (total cells that previously expressed AID) and AID.Cre.ERT2.tdTomato mice that received tamoxifen on day 10 of the response (cells that recently expressed AID). Flow cytometric analysis revealed that in both mouse models, very few $tdTomato^+$ B cells expressed CD138 (<2%; Fig. 3 B), demonstrating that a minor fraction of the $tdTomato^+$ B cells observed in LNs by whole-organ imaging are mature PCs. Although the imaging and flow cytometric data cannot be directly compared, the high number of Blimp-1 YFP^+ PCs in the LN cortex, and the small fraction detected by flow cytometry, may indicate that not all non-GC cells are recovered using the latter technique.

Flow cytometric analysis of $tdTomato^+$ B cells revealed two subpopulations that expressed CD38, a marker that is down-regulated in GC B cells (Oliver et al., 1997; Ridderstad and Tarlinton, 1998), and expressed either high or low levels of the activation marker FAS (Fig. 3 C). Similarly, flow cytometric analysis of cells derived from immunized AID.Cre.ERT2.tdTomato mice that were treated with tamoxifen revealed FAS^{Hi} and FAS^{Lo} B cell populations among the non-GC B cells (Fig. 3 C);

however, the frequency of the tdTomato$^+$CD38$^+$ FAS^{Lo} subpopulation was threefold smaller compared with AID.Cre.tdTomato mice. Similar analysis at early stages of the response revealed cells expressing tdTomato on day 3 after immunization that also expressed CD38 and low levels of FAS before GC formation (Fig. S4). Collectively, these results indicate that the recently AID-expressing cells that include post-GC cells are enriched in the FAS^{Hi} subset.

To further examine the identity of both the FAS^{Hi} and FAS^{Lo} CD38$^+$ tdTomato$^+$ B cells, we stained the cells for the typical memory cell markers PD-L2 and CD80 (Zuccarino-Catania et al., 2014). We found that in AID.Cre.tdTomato mice, ∼18% of the tdTomato$^+$ cells in both populations showed the typical memory cell phenotype, demonstrating that differentiation into memory cells is not specific for any one of these subpopulations. Similarly, analysis of cells derived from AID.Cre.ERT2.tdTomato mice revealed that 19% of the FAS^{Hi} cells expressed PD-L2 and CD80, whereas only 9% of the FAS^{Lo} cell population expressed these markers (Fig. 3, D and E). Collectively, these findings indicate that the majority of B cells that previously expressed AID early and late during the response do not show typical memory or PC indicators and may represent cells that are still part of the GC or post-GC cells that did not fully differentiate into PC or memory cells.

LZ B cells dynamically migrate within the GC outskirts, whereas the DZ boundary is a highly confined area

Our results, obtained by visualization of fixed LNs, revealed that most of the single B cells reside in the LN cortex, and very few cells are detected in the paracortex. Accordingly, examination of intact LNs and individual GC structures revealed that single cells are primarily found next to the area of the GCs that faces the LN cortex or the LN capsule, in an area known as the follicular mantle, and very few single B cells were detected in the area that faces the paracortex area (Fig. 4, A and B; and Video 4). This single-cell distribution pattern that surrounds the GC structures was observed throughout the immune response, at both early and late time points (Fig. 4 B). Similar analysis of individual GC structures in AID.Cre.ERT2.tdTomato mice that were treated with tamoxifen revealed that cells that express AID later during the response are enriched in the area of the follicular mantle that faces the outer edge of the LN (Fig. 4 B). Close analysis of individual GC surfaces at different time points revealed that the area of the GC that faces the outer part of the LN is very rough, whereas the side that faces the paracortex is smooth (Fig. 4 B, right panels; and Video 4). The LZ of the GC is enriched with a follicular dendritic cell network that faces the LN capsule (MacLennan, 1994; Heesters et al., 2014). By labeling the LZ with a fluorescent antigen (NP-tdTomato), we detected many single cells in proximity to the LZ and very few cells next to the DZ (Fig. 4 C).

Our observations suggest that the rough area of the GC is a site of actively migrating cells, whereas the smooth surface area represents a more confined zone. To address this possibility, we used a different type of pulse-chase experiment in living mice, by labeling cells in a specific zone of the GC followed by tracking the location of these cells after several hours. To this end, we crossed mice expressing a photoactivatable GFP (PA-GFP) transgene to mice that carry the B1-8^{hi} heavy chain allele. B1-8^{hi} B cells carry a knock-in Ig heavy chain that, when combined with an Igλ light chain, produces a BCR specific for NP (Shih et al., 2002; Victora et al., 2010). For clear visualization of the different GC zones by two-photon laser scanning microscopy, we used the prime-boost model wherein PA-GFP$^+$ B1-8^{hi} B cells were transferred to OVA-primed host mice before boosting with NP-OVA. To detect the GC LZ in vivo, we injected a fluorescent antigen (NP-tdTomato) that labels follicular dendritic cells (Victora et al., 2010). PA-GFP$^+$ B1-8^{hi} B cells were photoactivated in the LZ, and a three-dimensional (3D) volume surrounding the GC structure was imaged at 1-h intervals for 3–4 h (Fig. 4, D–F). At 1 h following photoactivation, we clearly detected a small number of activated PA-GFP$^+$ B1-8^{hi} B cells that had moved out from the LZ and migrated into its outskirts, and after an additional 3–4 h, ∼23% of the total detectable labeled cells were found outside the original photoactivated area. Most of the labeled cells were detected in very close proximity to the LZ boundary within the follicular mantle; however, few cells were clearly detected in close proximity to the LN capsule (Fig. 4 D and Video 5). Quantification of the increase in absolute cell number and frequency outside the GC over time suggested that the cells depart at a constant rate and accumulate in the LN cortex (Fig. 4, E and F). These findings demonstrate that B cells within the LZ are actively migrating within its proximal area and few cells constantly depart this area and move long distances within the LN cortex.

To examine the confinement of B cells in the DZ, we labeled by photoactivation the area that is proximal to the GC LZ facing the paracortex and contains autofluorescent macrophages. Two-photon laser scanning microscopy imaging of this area revealed a cluster of B1-8^{hi} B cells in close vicinity to the GC LZ that represents the DZ cells (Fig. 4 D). Tracking these cells over time revealed very few cells outside the DZ, whereas a significant number of photoactivated cells were found in the GC LZ after 4 h, as previously shown (Victora et al., 2010; Fig. 4, D–F). We conclude that the LZ is a permissive area through which B cells can dynamically migrate and enter the GC outskirts, whereas the DZ is a highly confined zone.

The number of single B cells in proximity to individual GC structures is highly variable

Using whole-organ imaging analysis allowed us to capture full GC structures for the first time and measure the number of cells in their vicinity. Close examination of individual GCs in a single LN revealed that different GC structures show considerable variation in numbers of cells located in their proximal area (Fig. 5 A). To roughly assess the number of cells next to individual GCs in a B cell follicle, we counted the number of single cells found in their proximity (Materials and methods). To measure the number of single B cells, relative to the GC size, we normalized the number of cells found outside the GC structures to the GC surface area (defined as the "proximity index"; Fig. 5, A and B). Quantification of the proximity index per GC in single LNs revealed highly variable numbers of B cells outside the GC structures in individual follicles. Some follicles showed many

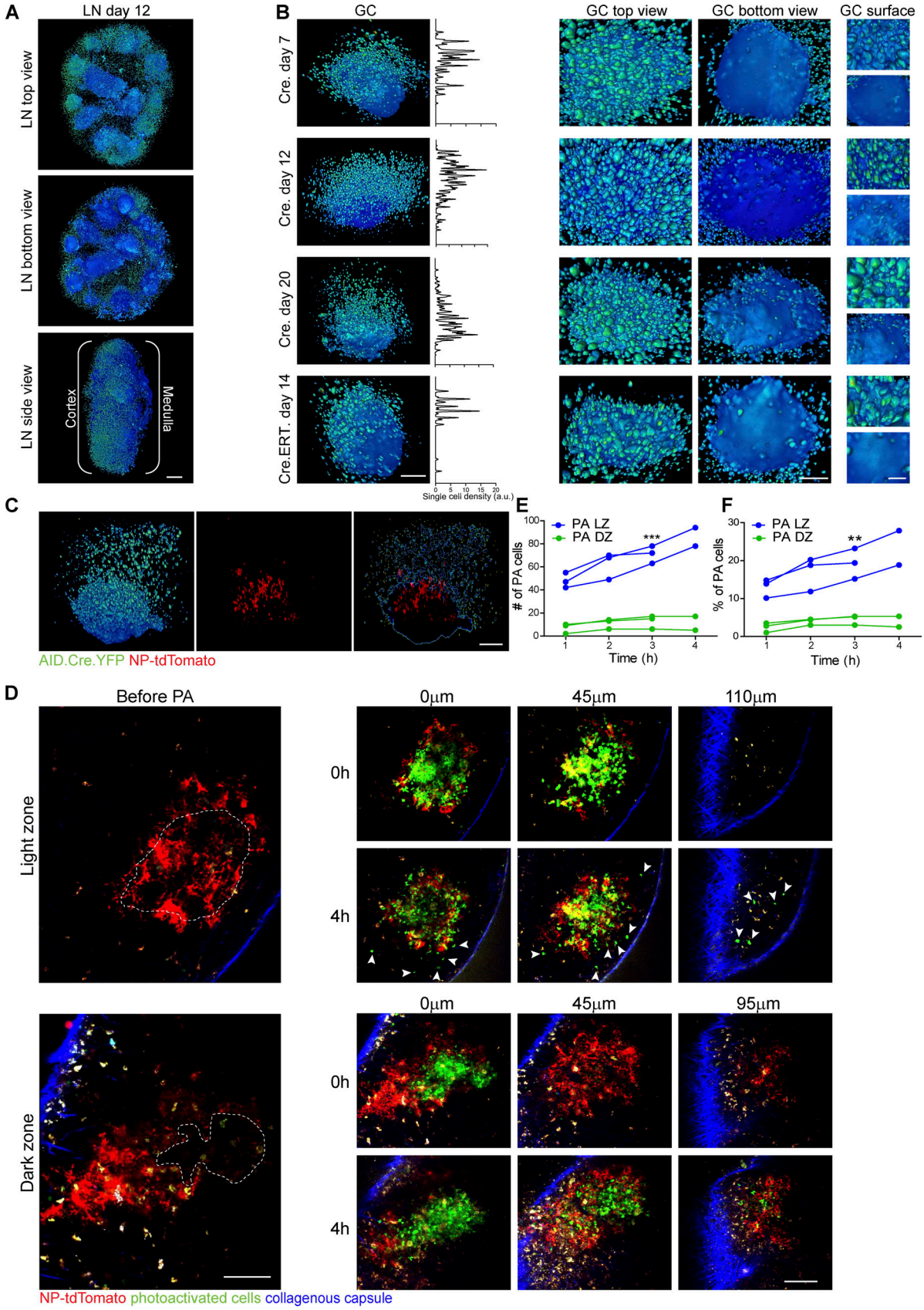

Figure 4. **LZ B cells migrate within the GC outskirts, whereas DZ B cells are highly confined to the GC. (A)** LSFM images of popliteal LNs dissected from AID.Cre.tdTomato mice 12 d after immunization with NP-OVA. Different orientations of the same LN are shown in 3D volumetric and rainbow visualization mode. Representative images from five independent experiments with a total of 21 LNs from 12 mice. Scale bar, 200 µm. **(B)** LSFM 3D-rendered images of

single GCs in different perspectives from AID.Cre.tdTomato (Cre) or AID.Cre.ERT2.tdTomato (Cre.ERT) mice that were immunized with NP-OVA. The graph indicates single-cell density across the GC. Magnification of top and bottom GC surfaces are shown in the right panels. Scale bar, 100 µm. Representative images of 70–212 GCs from 10 independent experiments with 4–12 mice per time point. Scale bar, 100 µm. **(C)** LSFM 3D-rendered images of a single GC from an AID.Cre.YFP mouse that was immunized with NP-OVA and 12 d after receiving NP-tdTomato 24 h before LN removal. Representative images of 96 GCs from three independent experiments with a total of four mice. Scale bar, 100 µm. **(D)** Time series showing position of B1-8^{hi} B cells expressing active PA-GFP, at different time points and locations after LZ (top panel) or DZ (bottom panel) photoactivation. The LZ is labeled with NP-tdTomato (red) within GCs of popliteal LNs of immunized live mice that received PA-GFP^{+} B1-8^{hi} B cells before immunization. Representative images of three mice from two independent experiments. Dotted lines depict the photoactivated area, and arrowheads indicate recently departed B cells from the photoactivated region. Scale bar, 100 µm. **(E and F)** Graphs showing numbers and percentages of active PA-GFP^{+} cells over time and position (quantification of cells in all the Z-stacks). Absolute cell number outside the GC over time (F) or the fraction of active PA-GFP^{+} cells out of the total photoactivated cells at time 0, found outside the GC (E). Analyzed data of three mice per group from two independent experiments. **, P < 0.01; ***, P < 0.0001; two-tailed Student's *t* test. a.u., arbitrary units.

tdTomato^{+} cells in the proximity of the GC, while others contained very few cells (Fig. 5 A). Time-course analysis revealed that the average number of cells in the vicinity of individual GCs did not change over time, and GCs with nearly no cells next to them were observed throughout the immune response (Fig. 5 B). These results indicate that the ability of B cells to enter the GC outskirts is highly heterogeneous among different GC structures throughout the immune response.

High-resolution analysis of the entire GC structure surface, including the areas that face the capsule and the paracortex, revealed considerable heterogeneity in the size and shape (Fig. 1, A and C). To measure GC surface roughness, we performed an analysis in which we excluded single cells from the 3D images and measured the surface curvature of large objects within the image that represent the GCs (roughness index; Fig. 5, A and C; and Materials and methods). In this analysis, the presence of single cells outside the GC structures did not affect the measurement; however, cells that were connected to the main GC body were considered as part of the GC surface area. We found that the relative surface curvatures were different among individual GCs, as some GCs showed a very smooth surface while others were relatively rough (Fig. 5, A and C). Furthermore, the roughness index strongly correlated with the number of cells found in proximity to the GC structure (Fig. 5 C). The presence of different numbers of single cells next to the rough area of the GC may suggest that these observations are related. To gain more insight about these possibilities, we repeated the experiments and examined the number of B cells proximal to the GC sites in AID.Cre.ERT2.tdTomato mice in which recently GC-departed cells are labeled. In analogy to the results obtained by imaging LNs of AID.Cre.tdTomato mice, we found that GCs in AID.Cre.ERT2.tdTomato mice that were treated with tamoxifen exhibited considerable variation in the number of cells positioned next to the GC structures (Fig. 5, D and E). Collectively, these findings provide an indication that confinement to the GC is variable among different GC structures within the same LN.

B cell dissemination within the LN cortex is regulated by BCR affinity

Competition during the GC reaction is based on relative BCR affinity, and B cells bearing low-affinity Igs form normal GCs only when B cells expressing high-affinity BCRs are absent (Shih et al., 2002; Schwickert et al., 2011). We examined whether B cells bearing low-affinity Igs enter the LN cortex as efficiently as their higher-affinity counterparts by comparing the presence of single NP-specific B cells expressing high (B1-8^{hi})- versus 40-fold-lower (B1-8^{lo})–affinity BCRs. To avoid competition with endogenous B cells in WT mice, we adoptively transferred B cells from BCR transgenic mice into primed mice that do not produce NP-specific B cells (MD4) followed by boosting with NP-OVA. To study fully developed GCs before the significant affinity increase in the B1-8^{lo} clones that occurs over time, intact LNs were dissected and subjected to LSFM imaging 10 d after the boost. As expected, both transgenic B cell types formed GCs (Fig. 6 A and Videos 6 and 7), and many B1-8^{hi} single B cells were detected throughout the LN cortex in MD4 host mice. Conversely, in LNs of mice that received B1-8^{lo} B cells, very few single cells were detected in the LN cortex, 3.7-fold fewer than in LNs that host B1-8^{hi} B cells (Fig. 6, A and B; and Videos 6 and 7). Calculation of single cell/GC volume ratio revealed that the decrease in single B1-8^{lo} cell number was not a result of changes in GC size (Fig. 6, B–D). By calculating the proximity index, we found that low-affinity GCs show 2.3-fold fewer B cells in their vicinity compared with GCs hosting high-affinity clones (Fig. 6 E). To examine whether the transgenic B cells gained affinity-increasing mutations during the GC response, we sorted single transferred GC cells and sequenced their *Igh* mRNA. This analysis revealed that only 13% of the B1-8^{lo} cells acquired the W33L mutation (Allen et al., 1988), 16% showed variation of the germline sequence without the W33L mutation, and the majority of the cells retained the loss of function mutations of the B1-8^{lo} *Igh* sequence (Fig. S5). These results indicate that the majority of the transferred B1-8^{lo} B cells indeed expressed BCRs that was lower in affinity compared with the transferred B1-8^{hi} B cells (Fig. S5). Thus, B cells bearing low-affinity BCRs can readily form GCs; however, these cells have a decreased capacity to enter the LN cortex.

CCR6 is required for effective B cell accumulation in the LN cortex

Positioning of B cells in the LN cortex likely involves changes in expression of G-coupled receptors that sense gradients of chemoattractants. CCR6 is important for formation of an intact memory compartment and effective recall response; however, it does not appear to play a major role in memory cell egress from GCs in the spleen (Wiede et al., 2013; Elgueta et al., 2015; Suan et al., 2017b). Although both the spleen and LNs host GCs in response to immune challenge, the spleen lacks the subcapsular sinus wherein CCL20, the ligand for CCR6, is expressed. We

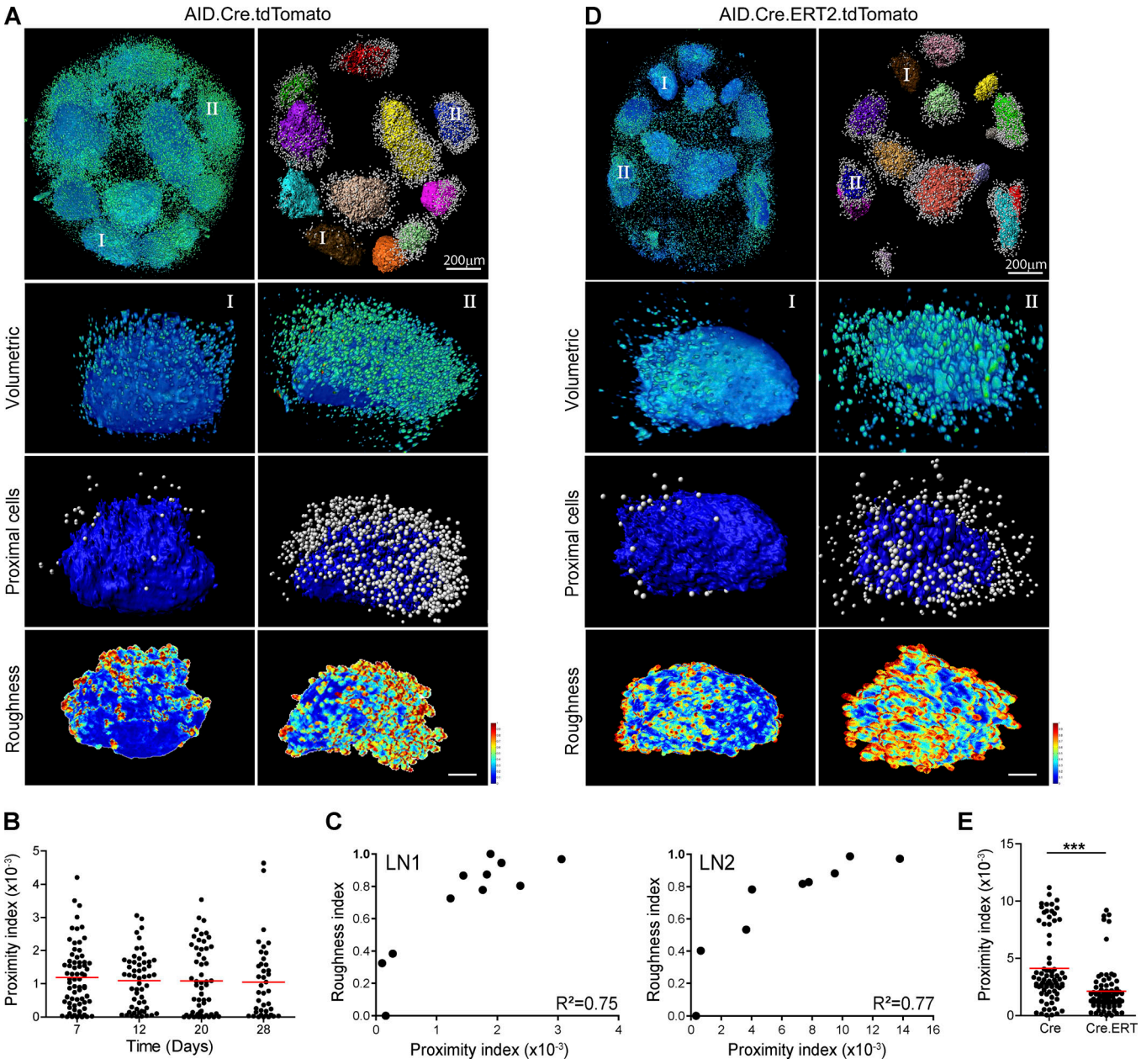

Figure 5. **The number of single B cells located next to individual GC structures is highly variable. (A)** LSFM 3D-rendered images of an LN removed from an immunized AID.Cre.tdTomato mouse (top left), and analysis for separate GCs (each GC is depicted in a different color) and individual B cells within 50 µm from each GC (top right). Higher magnification images of two GCs from the same LN, indicated by I and II, demonstrating volumetrics, proximal cells, and surface roughness analysis. Representative images from 5 independent experiments with a total of 21 LNs from 12 mice. Scale bar, 50 µm. **(B)** Quantification of the number of cells detected at a 50-µm distance from the GC, normalized to the GC surface area (proximity index) over time in AID.Cre.tdTomato mice. Data pooled from 3–5 independent experiments with a total of 4–21 LNs from 3–12 mice per group. **(C)** Correlation plots of roughness index (Materials and methods) and proximal index as measured for two representative single LNs. The R^2 values represent coefficients of determination. **(D)** LSFM 3D-rendered images of an LN removed from an immunized AID.Cre.ERT2.tdTomato mouse as in A that was treated with tamoxifen. Representative images from two independent experiments with eight LNs from four mice. Scale bar, 50 µm. **(E)** Quantification of proximity index as in B for GCs in AID.Cre.tdTomato (Cre) and AID.Cre.ERT2.tdTomato (Cre.ERT) mice 14 d after immunization with NP-OVA. Data pooled from two independent experiments with eight LNs from four mice per group. ***, $P < 0.0001$; two-tailed Student's *t* test.

used our whole-organ imaging approach to address the role of CCR6 in single B cell accumulation specifically in LNs. To this end, we imaged LNs from immunized AID.Cre.TdTomato $CCR6^{-/-}$ mice by LSFM (Fig. 7 A). We found 2.9-fold fewer single $tdTomato^+$ B cells in the LN cortex of $CCR6^{-/-}$ mice compared with $CCR6^{+/+}$ mice, suggesting that this receptor plays a key role in accumulation of B cells into the LN follicles at day 12 of the response (Fig. 7 B). Whole-organ imaging revealed that the GC size of $CCR6^{-/-}$ mice was slightly smaller than those in $CCR6^{+/+}$ mice (1.2-fold less; Fig. 7 C). However, normalization of the number of single B cells to the total GC size revealed a significant reduction in this ratio (2.3-fold) between $CCR6^{-/-}$ and $CCR6^{+/+}$

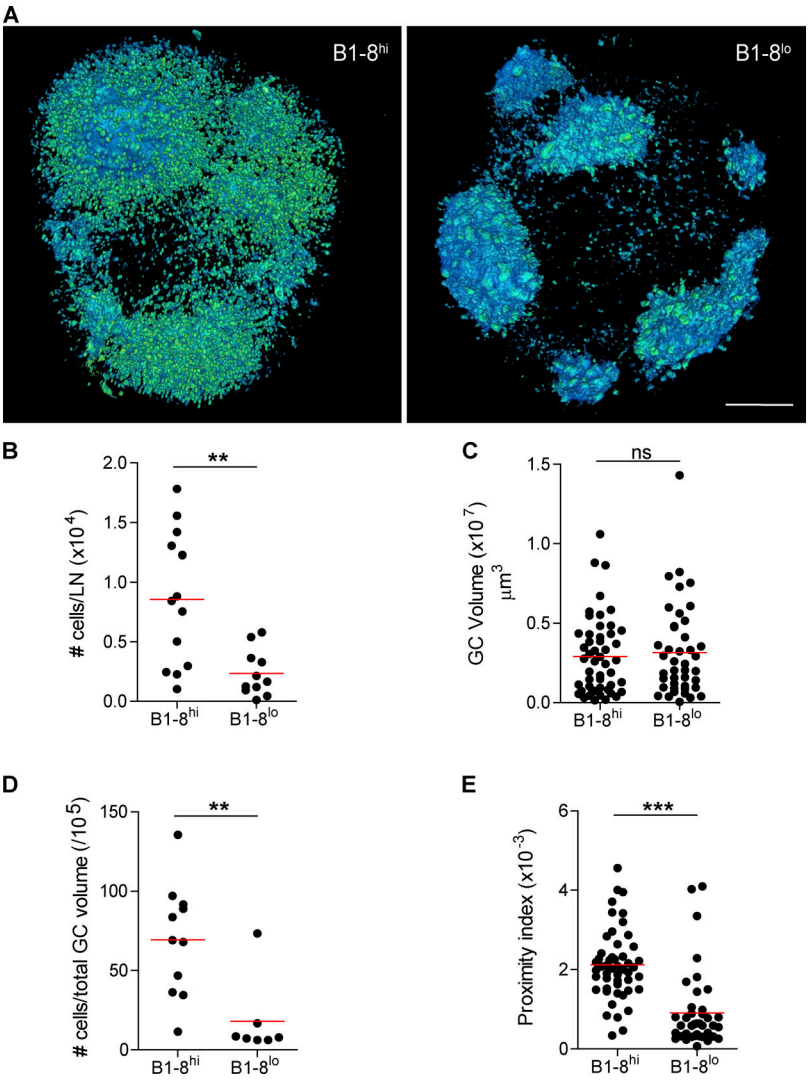

Figure 6. **B cell entry into the LN cortex is regulated by BCR affinity. (A)** Representative LSFM 3D-rendered images of LNs removed from immunized MD4 host mice that were adoptively transferred with DsRed$^+$ B1-8^{hi} or DsRed$^+$ B1-8^{lo} B cells. Scale bar, 200 µm. **(B–E)** Analysis of number of individual cells per LN (B), GC volume (C), number of non-GC individual cells normalized to the total GC volume (D), and proximity index (E). Representative images and data for A–E were pooled from three independent experiments with a total of 11–13 LNs from seven to eight mice per group. **, $P < 0.01$; ***, $P < 0.0001$; ns, not significant; two-tailed Student's *t* test.

mice, demonstrating that the presence of fewer single cells in CCR6$^{-/-}$ is not due to difference in the GC size (Fig. 7 D). Furthermore, analysis of the proximity index revealed 2.87-fold fewer B cells adjacent to the GCs in CCR6$^{-/-}$ mice (Fig. 7 E). We conclude that CCR6 is required for effective positioning of B cells in the LN cortex during early phases of the response.

Discussion

Visualization of an immune response in multiple microanatomical locations and niches at the level of a whole organ impose a major challenge. Using a large-scale imaging approach, we decoded the distribution patterns of B cells that previously expressed AID at different time points during the GC response, and obtained a detailed 3D map of their positions. As opposed to early-forming Blimp-1$^+$ and Irf4$^+$ PCs that transverse the T zone early during the response (Fooksman et al., 2010; Zhang et al., 2018), we show that the major path taken by most of the activated single B cells, including GC B cells at the peak and late stages of the response, is through the LN cortex. GC B cells are highly confined in the DZ, whereas LZ B cells migrate within the GC boundary within the mantle zone. Furthermore, we demonstrate that distinct BCR affinity thresholds regulate GC seeding and dissemination within the LN cortex.

Activated B cells within the LN follicles, including GC-departing cells, must migrate toward the efferent lymphatics in order to exit the LN and home to target tissues through the blood circulation (Mohr et al., 2009). Previous studies demonstrated the presence of PCs next to the GC DZ and migration of these cells toward the efferent lymphatic through the T cell zone early during the GC response. In addition, it was demonstrated that rare memory cells are positioned next to the LZ or the subcapsular sinus (Fooksman et al., 2010; Meyer-Hermann et al., 2012; Suan et al., 2017a; Moran et al., 2018; Zhang et al., 2018). Our analysis of B cell position around the entire GC structure revealed that most of the single cells were located next to the GC surface in an area that faces the LN capsule and encompasses the LZ, rather than next to the DZ area. The advantage of this type of analysis over traditional imaging approaches is that it allowed us to examine the GC structure in its entirety and compare B cell positions next to different parts of the GC niche in all the GCs in an intact LN. Many studies used CD38 in

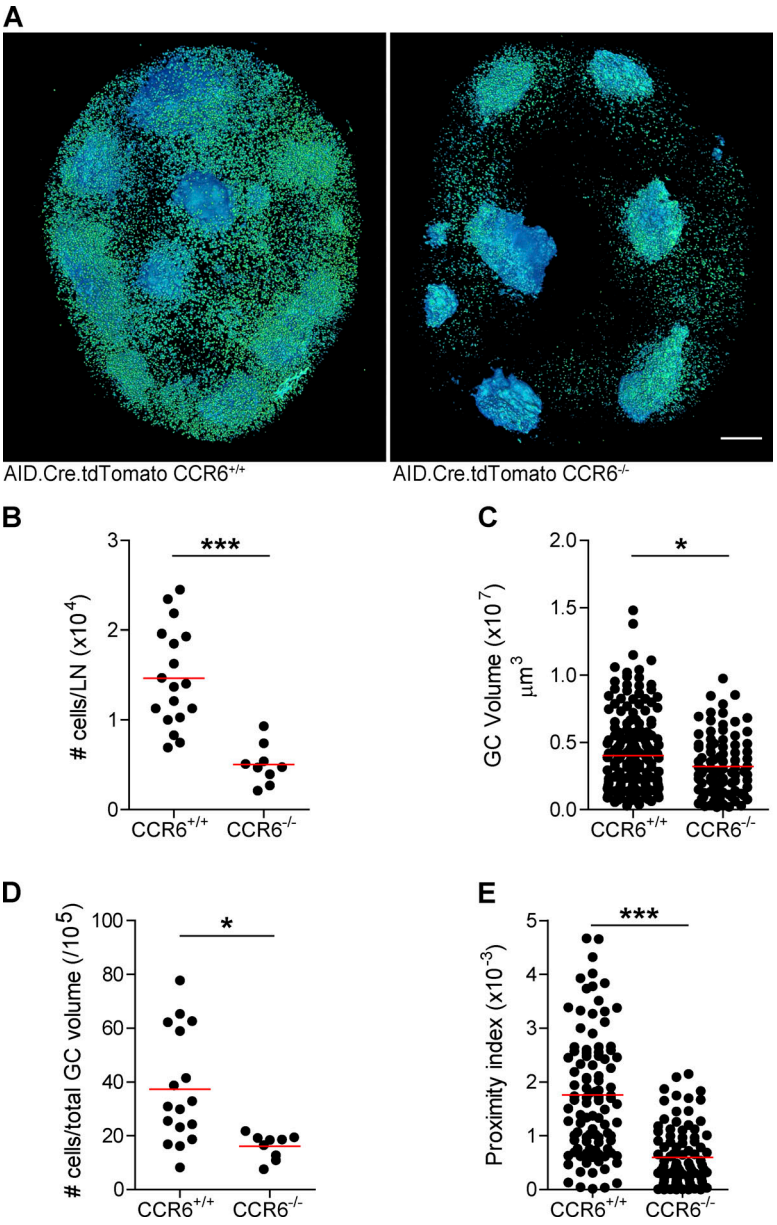

Figure 7. **CCR6 is required for efficient B cell entry into the LN cortex. (A)** Representative LSFM 3D-rendered images of LNs removed from AID.Cre.tdTomato or AID.Cre.tdTomato CCR6$^{-/-}$ mice 12 d after immunization with NP-OVA. Scale bar, 200 µm. **(B–E)** Analysis of the number of individual cells per LN (B), GC volume (C), number of non-GC individual cells normalized to the total GC volume (D), and proximity index (E). Representative images and data for A–E were pooled from three to five independent experiments with a total of 9–18 LNs from five to nine mice per group. *, P < 0.05; ***, P < 0.0001; two-tailed Student's *t* test.

combination with memory or IgG1 markers to define non-GC memory cells by flow cytometry, and some of these cells might be located next to the GC structure. Furthermore, the FAS$^+$ CD38$^+$ B cell subset that we detected by flow cytometry may represent an emerging population of cells that are located at the GC outskirts, rather than fully differentiated cells. Further investigation using techniques that combine spatial and transcriptomic analysis with commonly used cell surface markers are required to address this issue (Medaglia et al., 2017).

LZ B cells were found to move in the GC outskirts and migrate within the GC periphery. These findings suggest that GC departure involves a transitional retention at the GC outskirts, rather than direct movement from the GC into the follicles. This stage may include additional checkpoints that determine whether the cell will return to the GC or leave it. The outskirts of the LZ may contain the rare quiescent GC B cells that were found to down-regulate the GC transcription factor BCL6 and express early differentiation markers (Mueller et al., 2015; Kräutler et al., 2017; Laidlaw et al., 2017; Suan et al., 2017a; Wang et al., 2017).

In line with previous findings, using our imaging technique, we found that low-affinity clones seed GCs (Dal Porto et al., 2002; Shih et al., 2002; Schwickert et al., 2011); however, very few of these cells were able to enter the LN cortex, indicating that this process imposes a higher affinity threshold. It is possible that the increase in the BCR-dependent threshold during the GC reaction is a result of a diminishing amount of antigen throughout the response. In our experimental settings, although we used transgenic B cells, we could not compare how the exit of low-affinity clones changes over time since GC cells acquire affinity-enhancing mutations. Nonetheless, the amount of antigen is in constant decline, suggesting that the disadvantage of the low-affinity clones increases over time. Thus, we suggest that at the beginning of the response, a high level of antigen

promotes GC seeding by low- and high-affinity clones, and low levels of antigen during later time points of the response are sufficient to support primarily the departure of B cells bearing high-affinity BCRs. This mechanism can maintain GCs that accommodate low-affinity clones without allowing cellular egress and may provide the low-affinity clones or even B cells that do not show measurable antigen binding with sufficient time to accumulate somatic hypermutations and increase their antibody affinity (Shih et al., 2002; Kuraoka et al., 2016; Tas et al., 2016). Nonetheless, it was demonstrated that the majority of memory cells emerge from the low-affinity clones (Shinnakasu et al., 2016; Suan et al., 2017a; Weisel and Shlomchik, 2017). A possible explanation for this contradiction is that the B1-8^{lo} B cells may represent a very low-affinity clone that is very inefficient in differentiation into memory cells or PCs. Clones that do not show detectable binding to the antigen were found in GCs (Kuraoka et al., 2016; Tas et al., 2016), and our findings predict that these B cells will not be able to form memory or PC cells and exit the response. Collectively, these observations suggest that a minimal affinity threshold is required for entry of B cells into the follicles that is higher than the threshold of GC seeding.

The finding that GCs are heterogynous in size and in the number of proximal single cells suggests that more confined GC structures are unable to promote an efficient increase in antibody affinity (Tas et al., 2016). By normalizing the number of cells outside the GC structures to the total GC size, we found that the average single cell number in the LN cortex remained stable over time. However, when we compared high- and low-affinity transgenic B cells, we clearly detected an advantage for high-affinity clones in populating the LN cortex. These findings seem to contradict each other and suggest that other factors contribute to B cell accumulation and dissemination within the LNs. Indeed, the B cell reaction is constrained by negative factors that include reduction in antigen availability and increase in antibody concentration over time. These antibodies bind to inhibitory FcγRIIB receptors and block B cell interaction with antigen (Espéli et al., 2012; Zhang et al., 2013). Thus, our results suggest that although an increase in antibody affinity promotes PC generation (Phan et al., 2006), other limiting factors restrain it, leading to an almost unchanged net presence of single cells in the follicles over time.

Previous studies showed that CCR6 has a very small contribution to GC formation and compartmentalization (Reimer et al., 2017) and that CCR6 functions are dispensable for memory cell egress from GCs in the spleen (Elgueta et al., 2015; Suan et al., 2017a). Nonetheless, antibody formation in CCR6-deficient mice is severely reduced (Reimer et al., 2017). As opposed to the spleen, LSFM imaging of intact LNs revealed that the vast majority of egressing B cells depend on CCR6 expression for entry into the follicles (Elgueta et al., 2015; Reimer et al., 2017; Suan et al., 2017a). The LN is engulfed by the subcapsular sinus, whereas the spleen lacks this lymphatic endothelial vessel. CCL20, the CCR6 ligand, is expressed by lymphatic endothelial cells including the LN subcapsular sinus, suggesting that these cells attract the departing cells from the GC LZ toward the mantle zone (Zhang et al., 2016). CCR6 and possibly other chemokine receptors most likely guide GC-departing B cells from the cortex into lymphatic endothelial vessels that are found in close proximity to the B cell follicles (Kriehuber et al., 2001; Zhang et al., 2016). Indeed, it was demonstrated that naive B cells take this route as they egress the LN (Sinha et al., 2009). Since we did not delete CCR6 specifically in B cells, the role of other CCR6-expressing cells in this process cannot be completely excluded. Nonetheless, in agreement with previous studies, normal GCs were formed in CCR6-deficient mice. Furthermore, CCR6 might be dispensable for entry into the follicles in the case of an immune response elicited by stronger stimuli such as sheep red blood cells, or at later stages of the response (Elgueta et al., 2015; Suan et al., 2017a).

Collectively, here we demonstrate that imaging of intact organs provides a full picture of immune cell positioning and niche variation throughout the immune response. Understanding the cellular dynamics and molecular machineries that control PC and memory cell generation and egress is useful for vaccine design, as well as for intervention under pathological conditions such as in autoimmune diseases.

Materials and methods

Mice

AID.Cre.ERT2 mice were a kind gift from Prof. Claude-Agnes Reynaud (Institute Necker-Enfants Malades, Institut National de la Santé et de la Recherche Médicale, Paris, France). NP-specific B1-8^{hi} and B1-8^{lo} mice (Shih et al., 2002) were a kind gift from Prof. Michel Nussenzweig (The Rockefeller University, New York, NY). AID-GFP mice were generated by Prof. Rafael Casellas (National Institute of Arthritis and Musculoskeletal and Skin Diseases, National Institutes of Health, Bethesda, MD) and provided by Prof. Michel Nussenzweig. AID.Cre, Rosa26$^{flox\text{-}stop\text{-}flox\text{-}tdTomato}$, Rosa26$^{flox\text{-}stop\text{-}flox\text{-}YFP}$, Blimp-1-YFP, CCR6$^{-/-}$, PA-GFP^{+}, DsRed^{+}, CFP^{+}, GFP^{+}, and MD4 transgenic mice were purchased from the Jackson Laboratory. WT mice (C57BL/6) were provided by Harlan. All experiments with mice were approved by the Weizmann Institute Institutional Animal Care and Use Committee.

Adoptive cell transfers

B or T cells were purified by forcing spleen tissue through mesh into PBS containing 2% serum and 1 mM EDTA. Resting B cells were purified using anti-CD43 magnetic bead cell negative isolation kit, and T cells were purified using CD4^{+} negative isolation kit (Miltenyi). Following purification, 20–40 × 10^{6} GFP^{+} T cells or CFP^{+} B cells (as zone landmarks), or 3–5 × 10^{6} PA-GFP B1-8^{hi} (PA experiments) or 1.5 × 10^{6} B1-8^{hi} or 6 × 10^{6} B1-8^{lo} B cells (comprising 15% and 3%, respectively, Igλ^{+} NP-specific B cells; BCR affinity experiments) were transferred intravenously into host mice before immunization.

Immunizations and treatments

For primary immunization, mice were injected with 25 µl PBS containing 10 µg NP$_{16}$-OVA (Biosearch Technologies), precipitated in alum (Imject Alum; Thermo Scientific) at a 2:1 ratio, into the hind footpads. For T and B zone labeling, B and T cells were transferred 1 d before LN removal for imaging. In PA and BCR affinity experiments that involved adoptive cell transfer,

priming followed by boost immunizations was performed. WT mice or MD4 mice (6–10 wk of age) were given intraperitoneal injection of 50 µg OVA (Grade V; Sigma) in PBS and precipitated in alum (Imject Alum; Thermo Scientific) at a 2:1 ratio. 2 wk after priming, B cells were transferred into recipient mice that were boosted by injection of 25 µg soluble NP_{16}-OVA to the hind footpad. PA experiments were performed after 7 d, and BCR affinity experiments were performed 10 d after the boost. For imaging GC LZ, 1 µg NP conjugated to tdTomato was injected into the hind footpad ∼20 h before imaging. To activate Cre in AID.Cre.ERT2.tdTomato mice, tamoxifen in corn oil (15 mg/mouse; Sigma) was injected intraperitoneally 10 d after immunization with NP-OVA. Popliteal LNs were removed 4 d after tamoxifen or control (corn oil) injection. VSV (5×10^6 PFU; a kind gift from Dr. Matteo Iannacone, San Raffaele Scientific Institute, Milan, Italy) was injected into the hind footpad 14 d before LN removal. Chicken gamma globulin (10 µg; Biosearch Technologies) precipitated in alum (2:1) was injected into the hind footpads.

Flow cytometry

Single-cell suspensions were obtained by forcing popliteal LNs through a 70-µm mesh into ice-cold FACS buffer (EDTA 1 mM and 2% serum in PBS). Cells were incubated with 2 µg/ml anti-16/32 (clone 93) for blockage of Fc receptors for 5–10 min. Cell suspensions were washed and incubated with fluorescently labeled antibodies (B220 V500, FAS PE/Cy7, CD38 A700, CD138 BV605, CD80 APC, PD-L2 PC5.5; BioLegend) for 20–40 min. GC cells were gated as live/single, $B220^+$ $CD38^{Lo}$ FAS^{Hi}. PCs were defined as $B220^{med}$ $CD138^+$. $TdTomato^+$ cells were detected by the PE channel for AID.Cre.tdTomato and AID.Cre.ERT2.tdTomato. Cell suspensions were analyzed by Cytoflex (Beckman) flow cytometer.

LSFM imaging

Popliteal LNs were fixed in 1% paraformaldehyde for 1 h, followed by immersion in FocusClear (CelExplorer) for 2–7 d. Samples were imaged using a light sheet Z1 microscope (Zeiss Ltd.) equipped with two sCMOS cameras (PCO-Edge), 10× illumination objectives (LSFM clearing 10×/0.2) and Clr Plan-Neofluar (20×/1.0 Corr nd = 1.45), and detection objective dedicated for cleared samples in a water-based solution of final refractive index of 1.45. Samples were loaded into glass capillary in a 1.5% low melting agarose solution (Roth). Imaging was performed using dual-side illumination, with zoom 0.75, and multiview mode for tiling of multiple fields of view, with overlap of 10%. CFP excitation: 445; emission/detection: band pass (BP) 460–500; GFP excitation: 488; emission/detection: BP 505–545; RFP excitation: 561; emission/detection: BP 575–615.

Photoactivation and image acquisition

A Zeiss LSM 880 upright microscope fitted with a Coherent Chameleon Vision laser was used for intravital imaging experiments. Images were acquired with a femtosecond-pulsed two-photon laser tuned to 940 nm. The microscope was fitted with a filter cube containing 565 LPXR to split the emission to a PMT detector (with a 579–631-nm filter for tdTomato fluorescence) and to an additional 505 LPXR mirror to further split the emission to 2 GaAsp detectors (with a 500–550-nm filter for GFP fluorescence). GC LZ (labeled by NP-tdTomato) or DZ (facing the paracortex and containing autofluorescent macrophages) in the popliteal LN were photoactivated at 820 nm. Tile images were acquired as 100–200-µm Z-stacks with 5-µm steps between each Z-plane. The zoom was set to 1.5, and pictures were acquired at 512 × 512 x-y resolution.

BCR sequencing

Popliteal LNs from immunized MD4 mice were harvested and processed for flow cytometry analysis. Cell suspensions were stained for $dump^-$ (CD4 APC-eFluor, CD8 APC-eFluor, GR-1 APC-eFluor, F4/80 APC-eFluor) and B220 BV605, CD38 A700, GL-7 FITC, FAS PE/Cy7, Igλ APC, IgG1 BV421, and IgM PC5.5 (BioLegend). $TdTomato^+$ or $DsRed^+$ B cells were detected by the PE channel. Cell sorting was performed using a FACS Aria cell sorter (BD Bioscience). GC cells were gated as live/single, $B220^+$ $CD38^{Lo}$ FAS^{Hi}. GC-derived IgG1 B cells were sorted into 96 well plates containing lysis buffer (PBS with 3 U/µl RNAsin, 10 mM dithiothreitol). cDNA was purified using random primers (NEB) as previously described (Von Boehmer et al., 2016). Nested PCR was used to amplify a segment of Igγ1 heavy chains. $B1\text{-}8^{hi}$ or $B1\text{-}8^{lo}$ Igγ1 clones were amplified using the outer primers F (5′-GAG GAGACTGTGAGAGTGGTGCC-3′) and R (5′-CCATGGGATGGA GCTGTATCATCC-3′), followed by a second reaction with the inner primers F (5′-TGTGCTGGAGGGTTTGTCTAC-3′) and R (5′-TCACAGTAGCAGGCTTGAGG-3′). Amplification conditions were as follows: 94°C for 5 min, 50 cycles of 94°C for 30 s, 50°C for 30 s, and 72°C for 55 s (reaction I) or 50 s (reaction II), followed by 72°C for 10 min. The PCR products were sequenced and analyzed for CDR3 using the web-based IgBlast tool. Alignment to the germline sequence was performed using SnapGene software (GSL Biotech).

Image analysis

LSFM image dual-side fusion was performed using ZEN software (Zeiss). The independent tiles were stitched into a single image stack visualized in a volumetric mode with the rainbow color intensity gradient (for differential intensity between GCs and single cells) using Arivis Vision4D software. GC clusters with high intensities are encircled by neighboring cells with lower intensities, as the volume-rendering technique creates 3D objects from pixels based on the information about each pixel (position, size, and dimension). Quantification of GCs and individual B cells was done using Imaris software (Bitplane). First, both the GCs and the individual B cells from the same channel were segmented. The GCs were segmented by using the Imaris 3D surfaces module, and then single B cells were segmented using the Imaris spots module, after excluding the segmented GCs. When T zones and B cell follicles were marked with transferred GFP^+ T cells and CFP^+ B cells, the T zone was segmented as a surface based on the borders visualized by GFP^+ labeling, and the number of individual $tdTomato^+$ cells was quantified outside or within this surface, after excluding the segmented GCs. The number of B cells within a distance of 50 µm from each GC surface was quantified using Imaris

Find-Spots-Close-To-Surface extension. The 50-µm analysis was based on an observation acquired by two-photon microscopy, where an area that contains rapidly moving cells that are not part of the main GC body was detected. This area is relatively small, about the diameter of five cells. To measure the number of cells in this area, a 3D sphere was created around the entire GC surface, including both the DZ and LZ, and the number of cells between the GC surface and the sphere, all around the GC, was quantified. Background subtraction was applied before segmentation to enhance the signal. The assignment of a roughness score for a GC was based on an image-processing algorithm measuring local surface curvature. Images acquired using the LSFM were analyzed by Imaris as mentioned above, and a dedicated Imaris extension was developed using MATLAB (MathWorks). Single cells outside the GC were deleted, and the curvature measurement was done only on the structure of the GC, including LZs and DZs. The presence of single cells next to the GCs did not affect this analysis. However, the presence of "budding cells" that remain in contact with the GC structure is part of the measurement. The boundary of each GC was identified by a large number of points on its circumference. For each point, a set of nearest neighbors was identified, and a plane in 3D was fitted to this set. The SD of the neighbors' distance from this plane was used as a metric for local curvature. Points in a low-roughness region (smooth) would reside close to the plane and hence lead to a small SD and a roughness grade close to 0. Conversely, in a high-curvature region, points would deviate significantly from the plane, leading to a high roughness grade. Results from all GCs in each LN were normalized to the GC with maximal roughness, leading to a scale ranging from 0 to 1. To obtain a statistically stable result, a few hundred neighbors were used. A histogram describing the distribution of local curvature was constructed, and the local roughness in the 10th percentile of all points in the GC was used for the final roughness grade.

Online supplemental material

Fig. S1 shows the workflow for complete GC and single-cell analysis in intact LNs by whole-organ LSFM imaging. Fig. S2 shows that distinct immunological challenges induce GC responses that are similar to immunization with protein-conjugated hapten and that GC cells in AID reporter mice express GL-7. Fig. S3 shows GCs and single B cells in half an LN by LSFM. Fig. S4 shows the analysis of activated B cells early during the B cell response. Fig. S5 shows the Ig sequences of transgenic GC B cells. Video 1 shows LSFM imaging of a popliteal LN removed from an AID.Cre.tdTomato mouse 12 d after immunization with NP-OVA. Video 2 shows half an LN that was cut before its processing. Video 3 shows LSFM imaging of a popliteal LN removed from an AID.Cre.ERT2.tdTomato mouse treated with tamoxifen on day 10 after immunization and examined 4 d later. Video 4 shows LSFM imaging of a single GC. Video 5 shows intravital imaging of a popliteal LN 4 h after the LZ was photoactivated. Video 6 shows LSFM imaging of a popliteal LN removed from MD4 mice that received B1-8hi B cells, and Video 7 shows LSFM imaging of a popliteal LN removed from MD4 mice that received B1-8^{lo} B cells.

Acknowledgments

Z. Shulman is supported by the European Research Council grant no. 677713 and the Israel Science Foundation (2759/19). Z. Shulman is a European Molecular Biology Organization Young Investigator and is also supported by the Human Frontiers of Science Program (CDA-00023/2016), the Azrieli Foundation, the Rising Tide Foundation, the Morris Kahn Institute for Human Immunology, and grants from the Moross Integrated Cancer Center, the Comisaroff Family Trust, the Irma & Jacques Ber-Lehmsdorf Foundation, the Gerald O. Mann Charitable Foundation, and the David M. Polen Charitable Trust. Imaging was made possible thanks to "The de Picciotto-Lesser Cell Observatory in memory of Wolf and Ruth Lesser."

The authors declare no competing financial interests.

Author contributions: L. Stoler-Barak designed and conducted the experiments, performed data analysis, and wrote the manuscript. A. Biram and N. Davidzohn performed animal-related procedures. Y. Addadi assisted with light sheet imaging. O. Golani created the image quantification pipeline. Z. Shulman designed experiments, supervised the study, and wrote the manuscript.

Submitted: 2 May 2019
Revised: 2 July 2019
Accepted: 7 August 2019

References

Aiba, Y., K. Kometani, M. Hamadate, S. Moriyama, A. Sakaue-Sawano, M. Tomura, H. Luche, H.J. Fehling, R. Casellas, O. Kanagawa, et al. 2010. Preferential localization of IgG memory B cells adjacent to contracted germinal centers. *Proc. Natl. Acad. Sci. USA.* 107:12192–12197. https://doi.org/10.1073/pnas.1005443107

Allen, C.D.C., T. Okada, and J.G. Cyster. 2007. Germinal-center organization and cellular dynamics. *Immunity.* 27:190–202. https://doi.org/10.1016/j.immuni.2007.07.009

Allen, D., T. Simon, F. Sablitzky, K. Rajewsky, and A. Cumano. 1988. Antibody engineering for the analysis of affinity maturation of an anti-hapten response. *EMBO J.* 7:1995–2001. https://doi.org/10.1002/j.1460-2075.1988.tb03038.x

Biram, A., A. Strömberg, E. Winter, L. Stoler-Barak, R. Salomon, Y. Addadi, R. Dahan, G. Yaari, M. Bemark, and Z. Shulman. 2019. BCR affinity differentially regulates colonization of the subepithelial dome and infiltration into germinal centers within Peyer's patches. *Nat. Immunol.* 20:482–492. https://doi.org/10.1038/s41590-019-0325-1

Corcoran, L.M., and D.M. Tarlinton. 2016. Regulation of germinal center responses, memory B cells and plasma cell formation-an update. *Curr. Opin. Immunol.* 39:59–67. https://doi.org/10.1016/j.coi.2015.12.008

Crouch, E.E., Z. Li, M. Takizawa, S. Fichtner-Feigl, P. Gourzi, C. Montaño, L. Feigenbaum, P. Wilson, S. Janz, F.N. Papavasiliou, and R. Casellas. 2007. Regulation of AID expression in the immune response. *J. Exp. Med.* 204:1145–1156. https://doi.org/10.1084/jem.20061952

Dal Porto, J.M., A.M. Haberman, G. Kelsoe, and M.J. Shlomchik. 2002. Very low affinity B cells form germinal centers, become memory B cells, and participate in secondary immune responses when higher affinity competition is reduced. *J. Exp. Med.* 195:1215–1221. https://doi.org/10.1084/jem.20011550

De Silva, N.S., and U. Klein. 2015. Dynamics of B cells in germinal centres. *Nat. Rev. Immunol.* 15:137–148. https://doi.org/10.1038/nri3804

Eisen, H.N., and G.W. Siskind. 1964. Variations in affinities of antibodies during the immune response. *Biochemistry.* 3:996–1008. https://doi.org/10.1021/bi00895a027

Elgueta, R., E. Marks, E. Nowak, S. Menezes, M. Benson, V.S. Raman, C. Ortiz, S. O'Connell, H. Hess, G.M. Lord, and R. Noelle. 2015. CCR6-dependent positioning of memory B cells is essential for their ability to mount a recall response to antigen. *J. Immunol.* 194:505–513. https://doi.org/10.4049/jimmunol.1401553

Espéli, M., M.R. Clatworthy, S. Bökers, K.E. Lawlor, A.J. Cutler, F. Köntgen, P.A. Lyons, and K.G.C. Smith. 2012. Analysis of a wild mouse promoter variant reveals a novel role for FcγRIIb in the control of the germinal center and autoimmunity. *J. Exp. Med.* 209:2307–2319. https://doi.org/10.1084/jem.20121752

Fooksman, D.R., T.A. Schwickert, G.D. Victora, M.L. Dustin, M.C. Nussenzweig, and D. Skokos. 2010. Development and migration of plasma cells in the mouse lymph node. *Immunity.* 33:118–127. https://doi.org/10.1016/j.immuni.2010.06.015

Heesters, B.A., R.C. Myers, and M.C. Carroll. 2014. Follicular dendritic cells: dynamic antigen libraries. *Nat. Rev. Immunol.* 14:495–504. https://doi.org/10.1038/nri3689

Jacob, J., G. Kelsoe, K. Rajewsky, and U. Weiss. 1991. Intraclonal generation of antibody mutants in germinal centres. *Nature.* 354:389–392. https://doi.org/10.1038/354389a0

Kaji, T., A. Ishige, M. Hikida, J. Taka, A. Hijikata, M. Kubo, T. Nagashima, Y. Takahashi, T. Kurosaki, M. Okada, et al. 2012. Distinct cellular pathways select germline-encoded and somatically mutated antibodies into immunological memory. *J. Exp. Med.* 209:2079–2097. https://doi.org/10.1084/jem.20120127

Kallies, A., J. Hasbold, D.M. Tarlinton, W. Dietrich, L.M. Corcoran, P.D. Hodgkin, and S.L. Nutt. 2004. Plasma cell ontogeny defined by quantitative changes in blimp-1 expression. *J. Exp. Med.* 200:967–977. https://doi.org/10.1084/jem.20040973

Kräutler, N.J., D. Suan, D. Butt, K. Bourne, J.R. Hermes, T.D. Chan, C. Sundling, W. Kaplan, P. Schofield, J. Jackson, et al. 2017. Differentiation of germinal center B cells into plasma cells is initiated by high-affinity antigen and completed by Tfh cells. *J. Exp. Med.* 214:1259–1267. https://doi.org/10.1084/jem.20161533

Kriehuber, E., S. Breiteneder-Geleff, M. Groeger, A. Soleiman, S.F. Schoppmann, G. Stingl, D. Kerjaschki, and D. Maurer. 2001. Isolation and characterization of dermal lymphatic and blood endothelial cells reveal stable and functionally specialized cell lineages. *J. Exp. Med.* 194:797–808. https://doi.org/10.1084/jem.194.6.797

Kuraoka, M., A.G. Schmidt, T. Nojima, F. Feng, A. Watanabe, D. Kitamura, S.C. Harrison, T.B. Kepler, and G. Kelsoe. 2016. Complex antigens drive permissive clonal selection in germinal centers. *Immunity.* 44:542–552. https://doi.org/10.1016/j.immuni.2016.02.010

Laidlaw, B.J., T.H. Schmidt, J.A. Green, C.D.C. Allen, T. Okada, and J.G. Cyster. 2017. The Eph-related tyrosine kinase ligand Ephrin-B1 marks germinal center and memory precursor B cells. *J. Exp. Med.* 214:639–649. https://doi.org/10.1084/jem.20161461

MacLennan, I.C.M. 1994. Germinal centers. *Annu. Rev. Immunol.* 12:117–139. https://doi.org/10.1146/annurev.iy.12.040194.001001

Medaglia, C., A. Giladi, L. Stoler-Barak, M. De Giovanni, T.M. Salame, A. Biram, E. David, H. Li, M. Iannacone, Z. Shulman, and I. Amit. 2017. Spatial reconstruction of immune niches by combining photoactivatable reporters and scRNA-seq. *Science.* 358:1622–1626. https://doi.org/10.1126/science.aao4277

Meyer-Hermann, M., E. Mohr, N. Pelletier, Y. Zhang, G.D. Victora, and K.M. Toellner. 2012. A theory of germinal center B cell selection, division, and exit. *Cell Reports.* 2:162–174. https://doi.org/10.1016/j.celrep.2012.05.010

Mohr, E., K. Serre, R.A. Manz, A.F. Cunningham, M. Khan, D.L. Hardie, R. Bird, and I.C.M. MacLennan. 2009. Dendritic cells and monocyte/macrophages that create the IL-6/APRIL-rich lymph node microenvironments where plasmablasts mature. *J. Immunol.* 182:2113–2123. https://doi.org/10.4049/jimmunol.0802771

Moran, I., A. Nguyen, W.H. Khoo, D. Butt, K. Bourne, C. Young, J.R. Hermes, M. Biro, G. Gracie, C.S. Ma, et al. 2018. Memory B cells are reactivated in subcapsular proliferative foci of lymph nodes. *Nat. Commun.* 9:3372. https://doi.org/10.1038/s41467-018-05772-7

Mueller, J., M. Matloubian, and J. Zikherman. 2015. Cutting edge: An in vivo reporter reveals active B cell receptor signaling in the germinal center. *J. Immunol.* 194:2993–2997. https://doi.org/10.4049/jimmunol.1403086

Oliver, A.M., F. Martin, and J.F. Kearney. 1997. Mouse CD38 is down-regulated on germinal center B cells and mature plasma cells. *J. Immunol.* 158:1108–1115. https://doi.org/10.4049/jimmunol.174.2.817

Phan, T.G., D. Paus, T.D. Chan, M.L. Turner, S.L. Nutt, A. Basten, and R. Brink. 2006. High affinity germinal center B cells are actively selected into the plasma cell compartment. *J. Exp. Med.* 203:2419–2424. https://doi.org/10.1084/jem.20061254

Reimer, D., A.Y. Lee, J. Bannan, P. Fromm, E.E. Kara, I. Comerford, S. McColl, F. Wiede, D. Mielenz, and H. Körner. 2017. Early CCR6 expression on B cells modulates germinal centre kinetics and efficient antibody responses. *Immunol. Cell Biol.* 95:33–41. https://doi.org/10.1038/icb.2016.68

Ridderstad, A., and D.M. Tarlinton. 1998. Kinetics of establishing the memory B cell population as revealed by CD38 expression. *J. Immunol.* 160:4688–4695.

Rommel, P.C., D. Bosque, A.D. Gitlin, G.F. Croft, N. Heintz, R. Casellas, M.C. Nussenzweig, S. Kriaucionis, and D.F. Robbiani. 2013. Fate mapping for activation-induced cytidine deaminase (AID) marks non-lymphoid cells during mouse development. *PLoS One.* 8:e69208. https://doi.org/10.1371/journal.pone.0069208

Schwickert, T.A., G.D. Victora, D.R. Fooksman, A.O. Kamphorst, M.R. Mugnier, A.D. Gitlin, M.L. Dustin, and M.C. Nussenzweig. 2011. A dynamic T cell-limited checkpoint regulates affinity-dependent B cell entry into the germinal center. *J. Exp. Med.* 208:1243–1252. https://doi.org/10.1084/jem.20102477

Shih, T.-A.Y., E. Meffre, M. Roederer, and M.C. Nussenzweig. 2002. Role of BCR affinity in T cell dependent antibody responses in vivo. *Nat. Immunol.* 3:570–575. https://doi.org/10.1038/ni803

Shinnakasu, R., T. Inoue, K. Kometani, S. Moriyama, Y. Adachi, M. Nakayama, Y. Takahashi, H. Fukuyama, T. Okada, and T. Kurosaki. 2016. Regulated selection of germinal-center cells into the memory B cell compartment. *Nat. Immunol.* 17:861–869. https://doi.org/10.1038/ni.3460

Sinha, R.K., C. Park, I.Y. Hwang, M.D. Davis, and J.H. Kehrl. 2009. B lymphocytes exit lymph nodes through cortical lymphatic sinusoids by a mechanism independent of sphingosine-1-phosphate-mediated chemotaxis. *Immunity.* 30:434–446. https://doi.org/10.1016/j.immuni.2008.12.018

Suan, D., N.J. Kräutler, J.L.V. Maag, D. Butt, K. Bourne, J.R. Hermes, D.T. Avery, C. Young, A. Statham, M. Elliott, et al. 2017a. CCR6 defines memory B cell precursors in mouse and human germinal centers, revealing light-zone location and predominant low antigen affinity. *Immunity.* 47:1142–1153.e4. https://doi.org/10.1016/j.immuni.2017.11.022

Suan, D., C. Sundling, and R. Brink. 2017b. Plasma cell and memory B cell differentiation from the germinal center. *Curr. Opin. Immunol.* 45:97–102. https://doi.org/10.1016/j.coi.2017.03.006

Sze, D.M.-Y., K.-M. Toellner, C. García de Vinuesa, D.R. Taylor, and I.C.M. MacLennan. 2000. Intrinsic constraint on plasmablast growth and extrinsic limits of plasma cell survival. *J. Exp. Med.* 192:813–821. https://doi.org/10.1084/jem.192.6.813

Tas, J.M., L. Mesin, G. Pasqual, S. Targ, J.T. Jacobsen, Y.M. Mano, C.S. Chen, J.-C. Weill, C.-A. Reynaud, E.P. Browne, et al. 2016. Visualizing antibody affinity maturation in germinal centers. *Science.* 351:1048–1054. https://doi.org/10.1126/science.aad3439

Taylor, J.J., K.A. Pape, and M.K. Jenkins. 2012. A germinal center-independent pathway generates unswitched memory B cells early in the primary response. *J. Exp. Med.* 209:597–606. https://doi.org/10.1084/jem.20111696

Victora, G.D., and M.C. Nussenzweig. 2012. Germinal centers. *Annu. Rev. Immunol.* 30:429–457. https://doi.org/10.1146/annurev-immunol-020711-075032

Victora, G.D., T.A. Schwickert, D.R. Fooksman, A.O. Kamphorst, M. Meyer-Hermann, M.L. Dustin, and M.C. Nussenzweig. 2010. Germinal center dynamics revealed by multiphoton microscopy with a photoactivatable fluorescent reporter. *Cell.* 143:592–605. https://doi.org/10.1016/j.cell.2010.10.032

Von Boehmer, L., C. Liu, S. Ackerman, A.D. Gitlin, Q. Wang, A. Gazumyan, and M.C. Nussenzweig. 2016. Sequencing and cloning of antigen-specific antibodies from mouse memory B cells. *Nat. Protoc.* 11:1908–1923. https://doi.org/10.1038/nprot.2016.102

Wang, Y., J. Shi, J. Yan, Z. Xiao, X. Hou, P. Lu, S. Hou, T. Mao, W. Liu, Y. Ma, et al. 2017. Germinal-center development of memory B cells driven by IL-9 from follicular helper T cells. *Nat. Immunol.* 18:921–930. https://doi.org/10.1038/ni.3788

Weisel, F., and M. Shlomchik. 2017. Memory B cells of mice and humans. *Annu. Rev. Immunol.* 35:255–284. https://doi.org/10.1146/annurev-immunol-041015-055531

Wiede, F., P.D. Fromm, I. Comerford, E. Kara, J. Bannan, W. Schuh, C. Ranasinghe, D. Tarlinton, T. Winkler, S.R. McColl, and H. Körner. 2013. CCR6 is transiently upregulated on B cells after activation and modulates the germinal center reaction in the mouse. *Immunol. Cell Biol.* 91:335–339. https://doi.org/10.1038/icb.2013.14

Wittenbrink, N., A. Klein, A.A. Weiser, J. Schuchhardt, and M. Or-Guil. 2011. Is there a typical germinal center? A large-scale immunohistological study on the cellular composition of germinal centers during the hapten-carrier-driven primary immune response in mice. *J. Immunol.* 187:6185–6196. https://doi.org/10.4049/jimmunol.1101440

Zhang, T.T., D.G. Gonzalez, C.M. Cote, S.M. Kerfoot, S. Deng, Y. Cheng, M. Magari, and A.M. Haberman. 2017. Germinal center B cell development has distinctly regulated stages completed by disengagement from T cell help. *eLife.* 6:e19552. https://doi.org/10.7554/eLife.19552

Zhang, Y., M. Meyer-Hermann, L.A. George, M.T. Figge, M. Khan, M. Goodall, S.P. Young, A. Reynolds, F. Falciani, A. Waisman, et al. 2013. Germinal center B cells govern their own fate via antibody feedback. *J. Exp. Med.* 210:457–464. https://doi.org/10.1084/jem.20120150

Zhang, Y., T.L. Roth, E.E. Gray, H. Chen, L.B. Rodda, Y. Liang, P. Ventura, S. Villeda, P.R. Crocker, and J.G. Cyster. 2016. Migratory and adhesive cues controlling innate-like lymphocyte surveillance of the pathogen-exposed surface of the lymph node. *eLife.* 5:e18156. https://doi.org/10.7554/eLife.18156

Zhang, Y., L. Tech, L.A. George, A. Acs, R.E. Durrett, H. Hess, L.S.K. Walker, D.M. Tarlinton, A.L. Fletcher, A.E. Hauser, and K.M. Toellner. 2018. Plasma cell output from germinal centers is regulated by signals from Tfh and stromal cells. *J. Exp. Med.* 215:1227–1243. https://doi.org/10.1084/jem.20160832

Zuccarino-Catania, G.V., S. Sadanand, F.J. Weisel, M.M. Tomayko, H. Meng, S.H. Kleinstein, K.L. Good-Jacobson, and M.J. Shlomchik. 2014. CD80 and PD-L2 define functionally distinct memory B cell subsets that are independent of antibody isotype. *Nat. Immunol.* 15:631–637. https://doi.org/10.1038/ni.2914